Journal of Materials Chemistry A

Accepted Manuscript

ROYAL SOCIETY OF CHEMISTRY

www.rsc.org/materialsA

Monodispersed hollow aluminosilica microsphere @ hierarchical γ-AlOOH deposited with or without $Fe(OH)_3$ nanoparticles for efficient adsorption of organic pollutants

Yongxing Zhang[1], Yingjie Ye[3], Xiangbo zhou[1], Zhongliang Liu[1], Guangping Zhu[1], Dechuan Li[1] and Xuanhua Li[2*]

[1]Collaborative Innovation Center of Advanced Functional Composites, Huaibei Normal University, Huaibei 23500, P. R. China

[2] Center of Nano Energy Materials, State Key Laboratory of Solidification Processing, School of Materials Science and Engineering, Northwestern Polytechnical University Xi'an 710072, P. R. China

[3]School of Materials and Chemical Engineering, Henan Institute of Engineering, Zhengzhou, Henan 451191, P.R. China

E-mail: lixh32@nwpu.edu.cn

Abstract

Some conventional micro- or nano-structured adsorbents are subject to the problem that they can hardly show most of their adsorption sites for adsorbing pollutants in solution because of serious aggregation of adsorbents. Here, the monodispersed hollow aluminosilica microsphere (HAM) @ hierarchical γ-AlOOH nanomaterials have been firstly synthesized via a simple one-step template method. The positive charged $Fe(OH)_3$ colloid nanoparticles with a diameter of about 4nm have been effectively deposited onto the negatively charged surfaces of the hierarchical γ-AlOOH nanosheets to form the HAM@γ-AlOOH/$Fe(OH)_3$ with hierarchical structures via an electrostatic attraction without forming large aggregates. Both the HAM@γ-AlOOH and HAM@γ-AlOOH/$Fe(OH)_3$ with hierarchical structures have high specific surface areas and large pore volumes. The HAM@γ-AlOOH with the electronegative surface and the HAM@γ-AlOOH/$Fe(OH)_3$ with the electropositive surface are used as adsorbents to remove Methylene blue (MB) (cationic dye) and

Congo red (CR) (anionic dye) from aqueous solution, respectively. The maximum capacities of the monodispersed HAM@γ-AlOOH and HAM@γ-AlOOH/$Fe(OH)_3$ with hierarchical structures for MB and CR are determined at 87.80 mg g^{-1} and 252.53 mg g^{-1}, respectively, which are higher than those of the other metal oxide nanostructures reported to date. In addition, the adsorption rates of MB and CR onto the monodispersed HAM@γ-AlOOH and HAM@γ-AlOOH/$Fe(OH)_3$ with hierarchical structures are rather fast. This study also shows that the efficient adsorbents for organic pollution removal can be designed by depositing nanoparticles with high adsorption capacity on mesoporous supports with abundance of surface hydroxyls and large surface area.

Key words: hierarchical structures, organic pollution adsorption, aluminosilica microsphere, γ-AlOOH, $Fe(OH)_3$ nanomaterials

1. Introduction

In the past decade years, the synthesis of hollow nano and micro--structures with controllable morphology has attracted much attention for efficient removal of organic pollutants.[1-16] Many strategies have been developed to fabricate various hollow spheres.[17-23] Among the strategies, the template-directed synthetic method has proved to be the most effective route to produce inorganic hollow structures. For example, Lou et al. have successfully developed a simple sacrificial template method to synthesize uniform MS (M = Ni, Cu, Mn) hollow structures.[24] Our group use silica microspheres as templates to fabricate monodispersed hollow aluminosilica microspheres with thin shell structures.[25] In addition, silica nanospheres have also been widely used as hard templates, which obtained great success in the synthesis of mesoporous structures with various shell components and functional cores.[26-32]

Boehmite (γ-AlOOH) is widely used in catalysis,[33] adsorption,[34-36] catalyst supports,[37] and in the preparation of alumina-based materials.[38] Controlling the size and shape of γ-AlOOH

nanostructures plays a key role in improving the properties of the final alumina materials.[38, 39] Up to now, various hierarchically structured γ-AlOOH, such as three-quarter-sphere-like superstructures,[40] nanowire bunches,[41] hierarchically nanostructured microflowers,[42] rotor-like and carambola-like micro/nanoarchitectures[43] and spindle-like nanoarchitectures,[38] have been prepared. In addition, hollow γ-AlOOH microspheres have also been prepared. For example, Guan et al. have synthesized urchin-like boehmite hollow microspheres by using TX-100 as a surfactant.[44] Yu et al. have reported the template- and additive-free synthesis of hierarchically structured γ-AlOOH hollow spheres by the hydrothermal treatment of reaction mixtures containing potassium aluminium sulfate and urea.[35, 45] Buchold and Feldmann have synthesized nanoscale γ-AlOOH hollow spheres using water-in-oil (w/o) microemulsion templates.[46] However, there are few reports on the preparation of hollow monodispersed γ-AlOOH sphere with hierarchical structures by using silica microspheres as templates.

The positive charged $Fe(OH)_3$ colloid nanoparticles can be used as adsorbents for the removal of anion pollutant from water due to their large specific surface area and high available surface adsorption site density.[47] However, on the basis of practicality, the particles with nanometer size encounter some difficulties in the separation and recycling of the adsorbents from suspension after application in water and wastewater treatment, which hinders their industrial applications that are too fine to be removed by gravitational settling due to the strong Brownian motion. In addition, nanoparticles aggregation during adsorption processes limits their adsorption activity. Therefore, the search for $Fe(OH)_3$ colloid particles with high adsorption capacity, which can be easily separated from liquid phase by natural settlement in a short time is still a big challenge. In this work, the well-dispersed $Fe(OH)_3$ nanoparticles have been synthesized by using monodispersed hollow

aluminosilica microsphere(HAM)@γ-AlOOH with hierarchical structures as a adsorbent support.

To the best of our knowledge, this is the first report on the fabrication and adsorption capacity of hollow monodispersed HAM@γ-AlOOH and HAM@γ-AlOOH/$Fe(OH)_3$ composite hierarchical structures. Most importantly, these composite hierarchical structures in the efficient removal of organic pollution from water have the following features: (a) they are of low cost and nontoxic, which can be achieved by using low cost and nontoxic raw materials, and low cost synthesis methods; (b) their nanostructures provide the high surface area as well as the high removal capacity for organic pollution; (c) the monodispersed HAM@γ-AlOOH/$Fe(OH)_3$ with hierarchical structures, used as an adsorbent support, could prevent the agglomerate problem caused by high surface energy and Van der Waals force between the Fe(OH)3 colloid nanoparticles.

2. Experimental section

All reagents were of an analytical grade and are commercially available from Sinopharm Chemical Reagent Co., Ltd (China) and were used without further purification.

2.1. Preparation of monodispersed HAM@γ-AlOOH with hierarchical structures

In a typical experiment, silica microspheres (0.1 g) was dispersed to form a homogeneous suspension in deionized water (20 mL) by ultrasonication. Sodium aluminate ($NaAlO_2$) (1.0 g) and urea (2.88 g) were dissolved in 30 mL of deionized water by stirring. The above two solutions were then mixed to form a homogeneous suspension and transferred to a Teflon autoclave (70 mL) and heated to a temperature of 140 $^{\circ}$C for 6 h. After the reaction system was naturally cooled to room temperature, the white precipitates was separated from solution and thoroughly washed several times with

deionized water and absolutely ethanol, and then dried in a vacuum oven at 50 °C for 6 h.

2.2. Preparation of the monodispersed HAM@γ-AlOOH/Fe(OH)$_3$ with hierarchical structures

The monodispersed HAM@γ-AlOOH/Fe(OH)$_3$ with hierarchical structures were prepared by boiling forcing-hydrolysis method. In a typical synthesis, the negatively charged HAM@γ-AlOOH samples with hierarchical structures (50 mg) were well dispersed in deionized water (25 ml). Subsequently, the above solution was heated to boiling. Then, the saturated ferric chloride solution (5 ml) was added dropwise to the boiling solution. Continue to boil the solution until it became reddish brown, turn off the heat. After the reaction system was naturally cooled to room temperature, the precipitates was separated from solution and thoroughly washed several times with deionized water and absolutely ethanol, and then dried in a vacuum oven at 50 °C for 6 h.

2.3. Adsorption experiments

For the equilibrium adsorption isotherm study, the adsorption experiments were carried out in a serial of 15mL glass vials, equipped with aluminum foil-lined teflon screw caps. Adsorbents and MB or CR aqueous solution were added to the glass vial. Samples were shaken for 24h in order to achieve adsorption equilibrium. After the adsorption, adsorbents were separated using centrifugation. The adsorption capacity of the adsorbents was measured by the difference between the initial and remaining concentrations of MB or CR. The equilibrium adsorption capacity, q_e (mg g^{-1}), was calculated by $q_e = \frac{V(C_o - C_e)}{W}$, where C_o is the initial concentration of MB or CR (mg L^{-1}); C_e is the equilibrium concentration (mg L^{-1}); V is the volume of the solution used (L); and W is the weight of the adsorbents (g). The adsorption capacity of the adsorbents at time t, q_t (mg g^{-1}), was also

calculated: $q_t = \frac{V(C_o - C_t)}{W}$, where C_t is the concentration of MB or CR at contact time t (mg L^{-1}).

In the kinetic study of MB or CR adsorption on adsorbent samples, the initial MB or CR concentration was 15mg L^{-1}. The experiments were carried out using a 250mL conical flask containing 100mL of an MB or CR solution, and the adsorbent dose was 0.5g L^{-1} in the kinetics study. At predetermined time intervals, stirring was interrupted while 6mL of supernatant solutions were pipetted and centrifuged for the determination of the remaining MB or CR concentrations.

All the adsorption experiments were carried out at room temperature (298 ± 2 K). All the experimental data were the average of triplicate determinations. The relative errors of the data were about 5%.

2.4. Characterization

X-ray diffraction (XRD) patterns were obtained in the 2ɵ range of 10-90° using a Philips X'Pert Pro X-ray diffractometer with Cu Kα radiation (1.5418Å). Field emission scanning electron microscope (FESEM) images were taken on a FESEM (Quanta 200 FEG) operated at an accelerating voltage of 10.0kV. Transmission electron microscope (TEM) images were obtained on a JEOL JEM-2010 high resolution TEM, equipped with X-ray energy dispersive spectroscopy (EDS) capabilities, working at an acceleration voltage of 200kV. The specific surface areas of the samples were measured with Micromeritics ASAP 2020 $M^{+}C$ Brunauer-Emmet-Teller (BET) equipment by using nitrogen adsorption and desorption. The concentration of MB or CR in the solution was determined using a Shimadzu UV-2550 spectrophotometer.

3. Results and discussion

The phases of the SiO_2 microspheres and the as-prepared HAM@γ-AlOOH are examined by XRD. As shown in the curve (1) of Fig. 1 (a), the broad diffraction peak around 23° is ascribed to amorphous SiO_2.[48] The typical XRD pattern of the as-prepared HAM@γ-AlOOH is shown in the curve (2) of Fig. 1(a). According to our previous report, no peak can be observed for the HAM.[49] All of the diffraction peaks can be indexed to the orthorhombic γ-AlOOH (JCPDS 21-1307). Compared with the standard diffraction patterns, no characteristic peaks are from impurities.

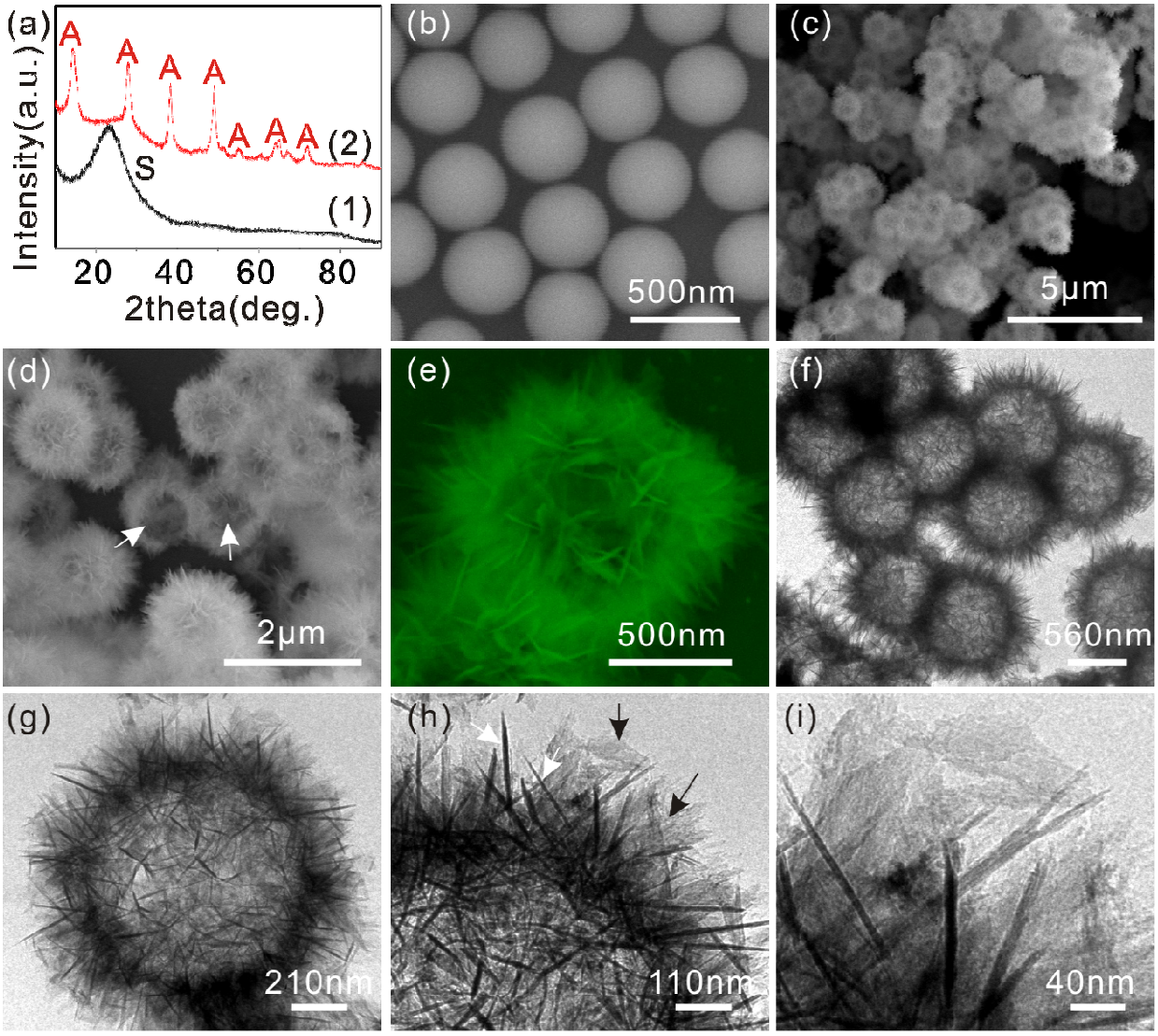

Figure 1. (a) XRD patterns of SiO_2 microspheres and as-prepared hierarchical HAM@γ-AlOOH with hierarchical structures. SEM images of (b) SiO_2 microspheres, (c), (d) and (e) HAM@γ

-AlOOH with hierarchical structures. TEM images of (f), (g), (h) and (i) HAM@γ-AlOOH with hierarchical structures,

Fig. 1 (b-e) shows SEM images of the SiO_2 microspheres and HAM@γ-AlOOH with hierarchical structures. Many monodispersed spherical SiO_2 with diameters of about 450 nm can be observed (Fig. 1 (b)). The surface of the SiO_2 microspheres is very smooth. After the SiO_2 microspheres are immersed in a mixed solution of $NaAlO_2$ and urea by the hydrothermal method, there are hairy-like structures on the surface of the microspheres, as shown in Fig. 1(c)-(e). Moreover, the mass production of uniform-sized sphere-like structures with diameters of about 1000nm can be observed. The SEM images (Fig. 1(d) and (e)) shows that the HAM@γ-AlOOH has hollow structures (indicated by the white arrows). The surface morphology of a single sphere can be clearly observed in the SEM image with a high magnification, as shown in Fig. 1(e). The whole hairy-like surface of the spherical particle is rough, which is composed of large amount of thin lamellas. TEM image (Fig. 1(f)-(i)) demonstrates that the uniform-sized spherical HAM@γ-AlOOH particles have hollow structures. The hierarchical structures of the spherical particles seem to be composed of many nanowires at first glance, as shown in Fig. 1(f) and (g). However, after careful observation, we could find that it is the edge of thin lamellas parallel to the electron beam (indicated by the white arrows in Fig. 1(h)), and many lamellar structures with an average thickness of about 6nm can be observed (indicated by the black arrows in Fig. 1(h)). High magnification TEM image further demonstrates that the hierarchical structures of the spherical particles are composed of lamellar structures, as shown in Fig. 1(i).

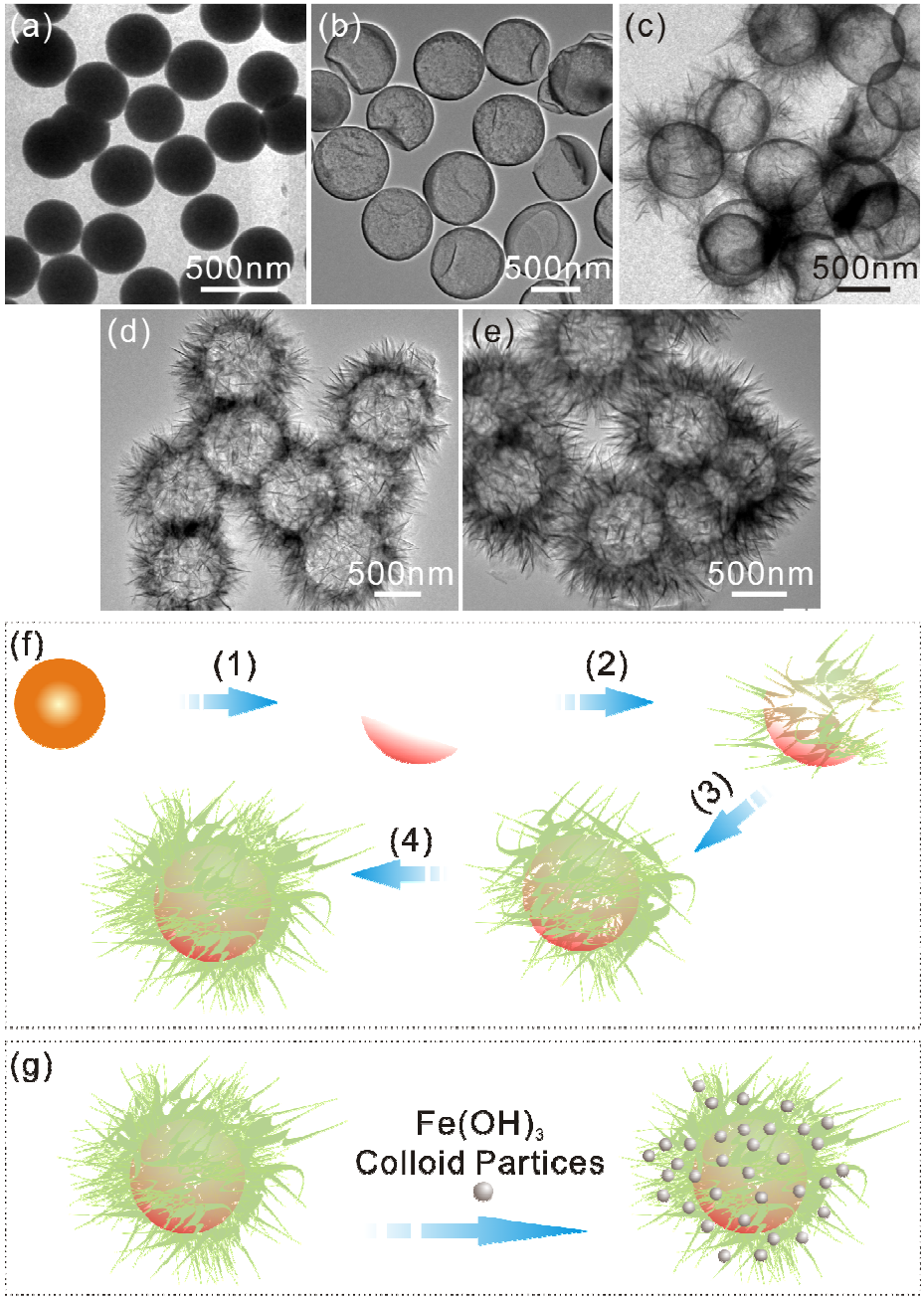

Figure 2. SEM images of the products HAM@γ-AlOOH collected at different reaction times: (a) 0 min, (b) 28 min, (c) 55 min, (d) 3h and (e) 6h. (f) Schematic illustration of the morphological evolution process of the HAM@γ-AlOOH with hierarchical structures. (g) Schematic illustration of boiling forcing-hydrolysis method for the formation of the HAM@γ-AlOOH/$Fe(OH)_3$ with hierarchical structures.

For the investigation of the formation process of the hollow HAM@γ-AlOOH nanospheres with hierarchical structures, experiments with different reaction duration are conducted and the corresponding products are examined using TEM, as shown in Fig. 2. The SiO_2 microspheres in the present experiment are 450nm in diameter with a smooth surface, as shown in Fig. 2(a). After 28min reaction, as shown in Fig. 2(b), HAMs with thin shell structures have been successfully synthesized. By increasing the hydrothermal time to 55 min, there are a few hairy-like lamellar structures appearing on the surface of the HAMs (Fig. 2(c)). However, the boundary of the HAMs is still can be observed. When the reaction time was prolonged to 3h, the HAM@γ-AlOOH with hierarchical structures is prepared. The hairy-like lamellar hierarchical structures become denser, as shown in Fig. 2(d). When the reaction is further increased to 6h (Fig. 2(e)), the product still exhibits the hairy-like lamellar hierarchical structures that are similar to the samples in Fig. 2(d), but the hairy-like lamellar hierarchical structures become much thicker. The morphology of the product does not change with longer reaction time.

On the basis of the time-dependent experiments, the formation of the HAM@γ-AlOOH with hierarchical structures can be rationally expressed as a self-assembly mechanism, as shown in Fig. 2(f). Generally, the aqueous solution having higher concentration of $NaAlO_2$ is strong alkaline. Before the decomposition of urea, the SiO_2 microspheres can be etched by the strong alkaline solution in our experiments. When the reaction time is 28 min, the HAMs can be obtained successfully (Fig. 1(b)).[49] When the urea starts to decompose, aluminate anions undergo the following chemical reactions:

$$AlO_2^- + 2H_2O \rightarrow Al(OH)_3 + OH^- \quad (1)$$

$$Al(OH)_3 \rightarrow \gamma\text{-}AlOOH + H_2O \quad (2)$$

In the present experiment, when the reaction time is prolonged to 55 min, $Al(OH)_3$ will be formed on the basis of the hydrolysis reaction through Eq.(1); the newly formed $Al(OH)_3$ is active and unstable, which will further dehydrate and convert into γ-AlOOH through Eq. (2), expectably. The growth process of the hairy-like lamellar hierarchical structures is therefore proposed as follows: In the reaction system, there is a large quantity of hydroxide ions. These ions can break the surface silicon-oxygen bonds of the HAMs. The silicon-oxygen bonds further induce the preferential hydrolysis of aluminate anions around the HAMs. The generated $Al(OH)_3$ colloids, which are unstable, convert gradually into γ-AlOOH according to Eq. (2) and then attaches onto the HAMs. As the reaction continue, more and more hairy-like lamellar structures are assembled together to form the entire HAM@γ-AlOOH with hierarchical structures.

The monodispersed HAM@γ-AlOOH with hierarchical structures can be used as an adsorbent support to synthesize other nanomaterilas, such as $Fe(OH)_3$. $Fe(OH)_3$ is a good material with positive charges on its surface, which has promising application in organic pollutants treatment. However, synthesis of well-dispersed $Fe(OH)_3$ nanomaterials is difficult. The nanomaterials easily aggregate, caused by high surface energy and Van der Waals force. In general, the surface properties of the HAM@γ-AlOOH are based on the presence of the functional groups. In near neutral aqueous environments, lamellar γ-AlOOH has a large number of surface hydroxyl groups. The groups cause the surface to have negatively charged due to the terminal OH sites. Thus, the positive charged $Fe(OH)_3$ colloid nanoparticles can be well effectively dispersed on the negatively charged surface of γ-AlOOH nanosheets via electrostatic attraction. As shown in Fig. 2 (g), the positive charged $Fe(OH)_3$ colloid nanoparticles can be effectively self-assembled onto the surfaces of the hierarchical γ-AlOOH nanosheets to form the HAM@γ-AlOOH/$Fe(OH)_3$ via an electrostatic attraction without

forming large aggregates.

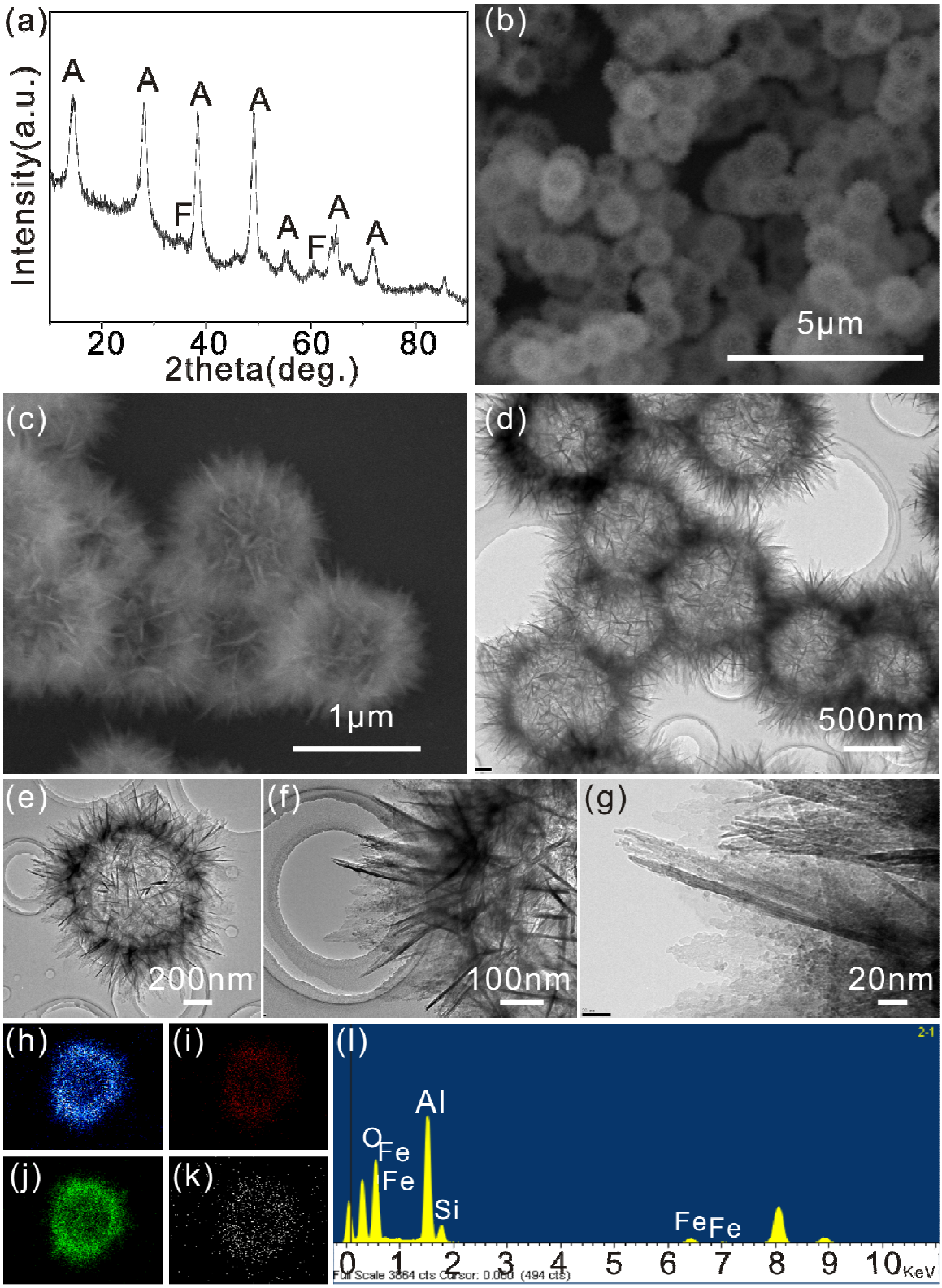

Figure 3. (a) XRD patterns, (b) and (c) SEM images, (d) TEM images of the

HAM@γ-AlOOH/$Fe(OH)_3$ microspheres with hierarchical structures. (e), (f) and (g) High-magnification TEM images of the HAM@γ-AlOOH/$Fe(OH)_3$ with hierarchical structures. Electron energy loss: (h) O, (i) Si, (j) Al and (k) Fe element mapping images of the HAM@γ-AlOOH/$Fe(OH)_3$ with hierarchical structures. (l) EDS data of the HAM@γ-AlOOH/$Fe(OH)_3$ with hierarchical structures

The as-prepared HAM@γ-AlOOH/$Fe(OH)_3$ with hierarchical structures have been comprehensively studied by using XRD, SEM, and TEM. Compared with the XRD pattern of HAM@γ-AlOOH show in Fig. 1(a), the XRD pattern of the HAM@γ-AlOOH/$Fe(OH)_3$ with hierarchical structures shows that additional peaks appear, which can be attributed to the phase of $Fe(OH)_3$ colloid nanoparticles (marked F in Fig. 3(a)). This suggests that the sample contains both γ-AlOOH and $Fe(OH)_3$ phases. However, because of the low content of $Fe(OH)_3$, the intensity of the XRD pattern of $Fe(OH)_3$ is very weak. Fig. 3(b), (c) and (d) show the SEM and TEM images of the HAM@γ-AlOOH/$Fe(OH)_3$ with hierarchical structures. From the figures, it is clear that the obtained products still maintain the uniform-sized, hollow and hierarchical structures. High-magnification TEM images are also used to examine the structures of the HAM@γ-AlOOH/$Fe(OH)_3$(Fig.3 (e)-(g)). Compared with Fig. 1(g)-(i), Fig.3 (e)-(g) clearly indicate that the positive charged $Fe(OH)_3$ colloid nanoparticles are successfully self-assembled on the negatively charged surface of the hierarchical γ-AlOOH nanosheets via electrostatic attraction. Careful examination of the high-magnification TEM micrographs (Fig.3 (g)) reveals that the $Fe(OH)_3$ colloid nanoparticles exhibit a relatively narrow size distribution with sizes ranging between 3 and 5 nm in diameter. These small size nanoparticles are well dispersed on the surface of the hierarchical γ-AlOOH nanosheets, which are more beneficial to further increasing the BET surface area of the HAM@γ-AlOOH/$Fe(OH)_3$ with

hierarchical structures. In order to further confirm the presence of the $Fe(OH)_3$ colloid nanoparticles on the surface of the HAM@γ-AlOOH/$Fe(OH)_3$, samples are analyzed by electron mapping image analysis (Fig.3 (h)-(k)). The images are acquired by visualizing the inelastically scattered electrons in the energy loss windows for elemental O, Si, Al, and Fe. The different color areas shown in Fig.3 (h)-(k) indicate O-, Si-, Al-, and Fe-enriched areas of the sample, respectively. The images also show that the $Fe(OH)_3$ colloid nanoparticles are well dispersed on the surface of the HAM@γ-AlOOH. The energy dispersive spectroscopic (EDS) analysis (Fig. 3(i)) of the HAM@γ-AlOOH/$Fe(OH)_3$ reveals the existence of O, Si, Al, and Fe elements. In addition, the exact loading of $Fe(OH)_3$ nanoparticles (mol %) is 6.33, which has been characterized by the inductively coupled plasma mass spectrometry (Agilent7500CS).

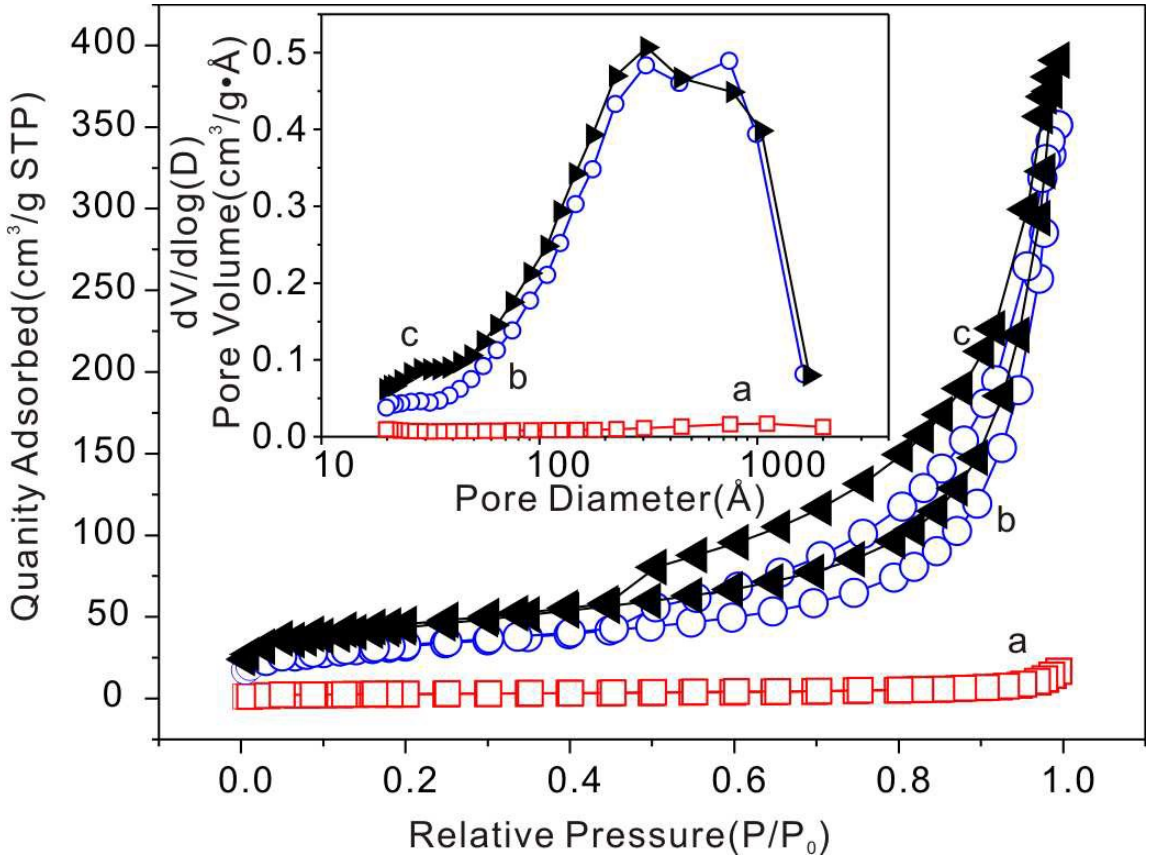

Figure 4. Nitrogen adsorption-desorption isotherms and the corresponding pore size distribution

curves (inset) of a) SiO_2 microspheres, b) HAM@γ-AlOOH with hierarchical structures and c) HAM@γ-AlOOH/$Fe(OH)_3$ with hierarchical structures.

Table 1. Physical properties of the different samples

Samples	BET (m^2 g^{-1})	Average pore diameter (nm)	Pore volume (cm^3 g^{-1})
SiO_2 microspheres	9.6	6.49	0.016
HAM@γ-AlOOH with hierarchical structures	114.3	13.9	0.398
HAM@γ-AlOOH/$Fe(OH)_3$ with hierarchical structures	154.9	11.8	0.455

The texture of the as-prepared sample is characterized by N_2 physisorption experiments and the corresponding N_2 adsorption-desorption isotherms, and pore size distributions are shown in Fig. 4. It is clear that both the HAM@γ-AlOOH and the HAM@γ-AlOOH/$Fe(OH)_3$ have type IV isotherms, suggesting that they have meso/macroporous structures. For the HAM@γ-AlOOH, the pore size distribution curve exhibits a broad peak in the range of 7-100 nm with a maximum at 30 nm. For the HAM@γ-AlOOH/$Fe(OH)_3$, the pore size distribution curve exhibits a broad peak in the range of 6-100 nm with a maximum at 30 nm. The results indicate that there are some mesopores/macropores in both of the samples. The mesopores reflect porosity between the γ-AlOOH nanosheets which form the HAM@γ-AlOOH or HAM@γ-AlOOH/$Fe(OH)_3$, while larger mesopores/macropores can be related to the pores formed between the HAM@γ-AlOOH or HAM@γ-AlOOH/$Fe(OH)_3$. However, the porous nature of the SiO_2 microspheres can be neglected. These mesoporous/macroporous structures can be also directly observed from the SEM and TEM images of the products shown in Fig. 1 and 3. The quantitative texture information of the as-synthesized samples, such as BET surface areas, average pore diameters and pore volumes, are summarized in Table 1. From the data, we can

see that the HAM@γ-AlOOH with hierarchical structures possess a large BET surface area and a high pore volume. After the deposition of positive charged $Fe(OH)_3$ colloid nanoparticles with a diameter of about 4nm, the BET surface area and pore volume of the HAM@γ-AlOOH/$Fe(OH)_3$ with hierarchical structures is larger than that of the HAM@γ-AlOOH with hierarchical structures. The SiO_2 microspheres have the smallest BET surface area and pore volume. The high BET surface area, high value of pore volume and ideal pore size distribution allow the HAM@γ-AlOOH and HAM@γ-AlOOH/$Fe(OH)_3$ with hierarchical structures as promising candidates for application in organic pollution removal from water.

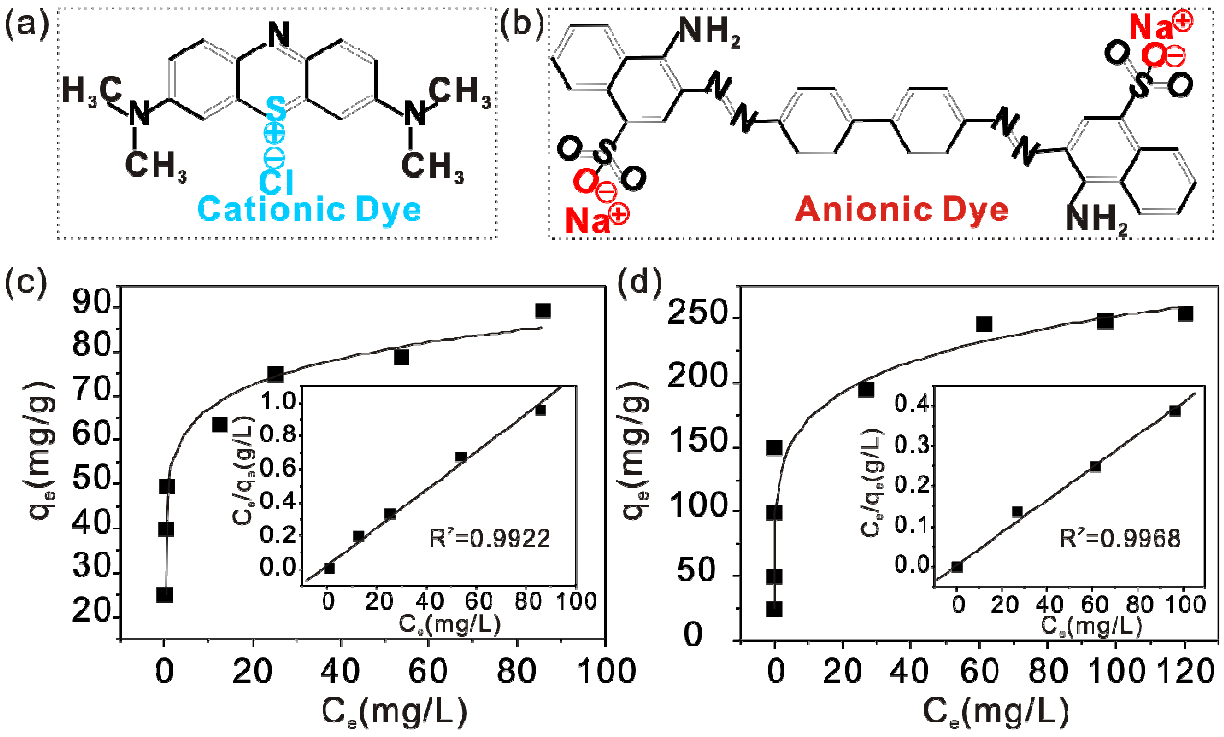

Figure 5. The chemical structures of (a) MB (Cationic Dye) and (b) CR (Anionic Dye). Adsorption isotherms of (c) MB and (d) CR adsorbed by the HAM@γ-AlOOH and HAM@γ-AlOOH/$Fe(OH)_3$ with hierarchical structures; The insets of (c) and (d) show plots of C_e versus C_e/q_e for the adsorption isotherms with Langmuir isotherm model.

To investigate the potential application of the monodispersed HAM@γ-AlOOH with the electronegative surface and the monodispersed HAM@γ-AlOOH/$Fe(OH)_3$ with the electropositive surface in water purification, we select the MB (cationic dye) and CR (anionic dye) to evaluate the ability of organic pollutants removal (see Fig. 5 (a) and (b) for their chemical structures). The presences of these dyes in water, even at very low concentrations, are highly visible and undesirable, causing environmental and health problems to human beings and aquatic animals. Adsorption is an effective way for the treatment of the dyes in wastewaters. Actually, in our experiments, it is found that the HAM@γ-AlOOH has no adsorption for CR, while the HAM@γ-AlOOH/$Fe(OH)_3$ has weak adsorption for MB. Fig. 5 (c) and (d) show the adsorption isotherms of MB and CR adsorbed by the monodispersed HAM@γ-AlOOH and HAM@γ-AlOOH/$Fe(OH)_3$ with hierarchical structures at room temperature, respectively. The equilibrium adsorption amounts increase sharply with increasing equilibrium concentration and reach saturation quickly. The Langmuir isotherm model is used to analyze the experimental data. The mathematical expression of the Langmuir isotherm is expressed as Eq. (3): [42, 50]

$$q_e = C_e q_m K_L / (1 + C_e K_L) \quad (3)$$

where q_e (mg g^{-1}) is the equilibrium adsoption amount, C_e (mg L^{-1}) is the equilibrium concentration, q_m (mg g^{-1}) is the maximum adsorption amount, and K_L is the equilibrium adsorption constant. Eq. (3) can be converted to Eq. (4):

$$C_e / q_e = 1 / q_m K_L + C_e / q_m \quad (4)$$

The maximum capacities of the monodispersed HAM@γ-AlOOH and HAM@γ-AlOOH/$Fe(OH)_3$ with hierarchical structures for MB and CR are determined at 87.80 mg g^{-1} and 252.53 mg g^{-1}, respectively. Both the two adsorbents can remove the organic ions from solution via electrostatic

attraction mechanisms. The insets of Fig. 5(c) and (d) show the plots of C_e versus C_e/q_e for the adsorption isotherms. Good fittings can be obtained and the correlation coefficients are 0.9922 and 0.9968 for the both curves. From the correlation coefficients, it can be seen that the adsorption data of the monodispersed HAM@γ-AlOOH and HAM@γ-AlOOH/$Fe(OH)_3$ with hierarchical structures for MB and CR fit the Langmuir isotherm model very well. In addition, the final adsorption capacities of HAM@γ-AlOOH collected at different reaction times and the effects of different loadings of $Fe(OH)_3$ nanoparticles on the adsorption efficiency of the HAM@γ-AlOOH have been investigated, and the results are shown in Figure S1 and S2. The HAM@γ-AlOOH and HAM@γ-AlOOH/$Fe(OH)_3$ have also been used for adsorbent of kinds of organic pollutants, such as Rhodamine 6G (R6G, cationic dye) and Methyl orange (MO, anionic dye), as shown in Figure S3.

Table 2. Comparison of our work with some metal oxides reported for the removal of MB and CR.

Adsorbents	q_m (mg g-1)		References
	MB	CR	
HAM@γ-AlOOH with hierarchical structures	87.80	–	This study
hierarchical porous MgO	82.70	–	51
Hexagonal WO_3 nanorod	73.00	–	52
TiO_2 nanotubes	57.14	–	53
Nanostructured Mn_3O_4	53.80-70.00	–	54
ZnO/$ZnFe_2O_4$ particles	37.27	–	55
HAM@γ-AlOOH/$Fe(OH)_3$ with hierarchical structures	–	252.53	This study
Spindle-like γ-Al_2O_3	–	176.70	38
Nanorod-like γ-Al_2O_3	–	83.80	56
Porous ZrO_2 hollow spheres	–	59.50	57
MnO_2 hierarchical hollow nanostructures	–	60.00	58

Mesoporous Fe_2O_3	—	53.00	59

To assess the organic dyes removal performance of both the two adsorbents, the adsorption capacities of the monodispersed HAM@γ-AlOOH and HAM@γ-AlOOH/$Fe(OH)_3$ with hierarchical structures for MB and CR are compared with other metal oxide nanostructures. Table 1 indicates that the adsorption capacities of the monodispersed HAM@γ-AlOOH and HAM@γ-AlOOH/$Fe(OH)_3$ with hierarchical structures for MB and CR in this study are higher than those of the other metal oxide nanostructures reported to date. For instance, the adsorption capacities of the porous ZrO_2 hollow sphere for CR is just 59.5 mg g^{-1}, while the adsorption capacities of the monodispersed HAM@γ-AlOOH/$Fe(OH)_3$ with hierarchical structures in this study for CR are 252.53 mg g^{-1}, which is about 4.2 times than that of the porous ZrO_2 hollow spheres. The high adsorption capacity is due to the higher specific area and novel hollow nanostructures.

The kinetics of adsorption, which describes the solute uptake rate governing the residence time of the adsorption reaction, is one of the most important characteristics that define the efficiency of adsorption. The kinetics curves of MB and CR adsorption onto the monodispersed HAM@γ-AlOOH and HAM@γ-AlOOH/$Fe(OH)_3$ with hierarchical structures are shown in Fig. 6 (a) and (b). Obviously, the adsorption rates of MB and CR are rather fast. In such experimental conditions, most MB and CR could be removed after 1 h. The very good monodispersity and the large BET surface area for the HAM @ γ-AlOOH or HAM @ γ-AlOOH/$Fe(OH)_3$ may be the main reasons for the fast removal of the organic pollutions. The above adsorption kinetic experimental data can be best fitted into a pseudo-second-order rate kinetic model. The pseudo-second-order model is presented as Eq. (5) [60, 61]:

$$t/q_t = 1/K_2 q_e^2 + t/q_e \qquad (5)$$

where q_e and q_t are the amount of MB and CR adsorbed at equilibrium and at time t, respectively. K_2 is the rate constant of the pseudo-second-order model of adsorption (g mg^{-1} min^{-1}). For the pseudo-second-order model, the values of K_2 and q_e can be obtained by a plot of t/q_t against t. The pseudo-second-order kinetics plots for the adsorption of MB and CR onto the monodispersed HAM@γ-AlOOH and HAM@γ-AlOOH/$Fe(OH)_3$ with hierarchical structures are shown in the insets of Fig 6 (a) and (b). The insets demonstrate that the experimental data could be well fitted with the linear form of the pseudo-second-order model. The correlation coefficient values for the pseudo-second-order model are all above 0.9998, suggesting that the pseudo-second-order model best represents the adsorption kinetics in our adsorbent systems.

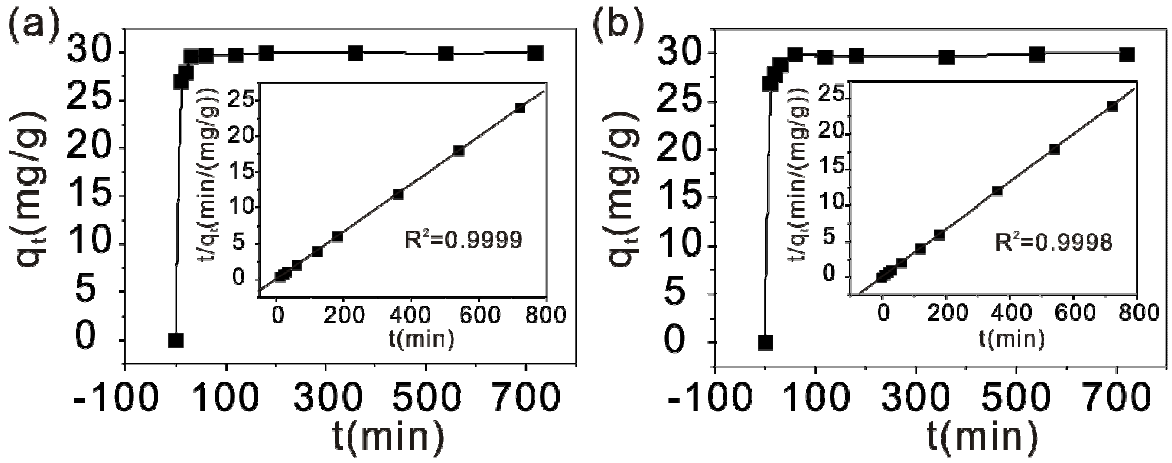

Figure 6. Adsorption kinetics curves of (a) MB and (b) CR adsorbed by 50mg of the HAM@γ-AlOOH with hierarchical structures and 50mg of the monodispersed HAM@γ-AlOOH/$Fe(OH)_3$ with hierarchical structures. The initial concentrations of MB and CR are both 15mg L^{-1}. The insets of Figure 6 (a) and (b) show the plots of t versus t/qt for the adsorption kinetics with the pseudo-second-order model.

4. Conclusions

In summary, we have used $NaAlO_2$, a nontoxic and inexpensive reagent, to synthesize the monodispersed HAM@γ-AlOOH with hierarchical structures by a simple hydrothermal method. The formation mechanism of the as-prepared sample is clarified by investigating the morphology evolution process. In addition, by adopting the as-prepared HAM@γ-AlOOH structure as a support and using ferric chloride as the iron resource, the well-distributed $Fe(OH)_3$ nanoparticles are obtained and coated onto HAM@γ-AlOOH surface by the boiling forcing-hydrolysis method. The monodispersed HAM@γ-AlOOH/$Fe(OH)_3$ hierarchical structures show the advantages of both microstructure and nanostructure, which can avoid aggregation of $Fe(OH)_3$ nanoparticles and maintain the high specific surface areas, high value of pore volume and ideal pore size distribution. Furthermore, the two novel micro/nanocomposite structures HAM@γ-AlOOH and HAM@γ-AlOOH/$Fe(OH)_3$ show high adsorption capacity for methylene blue (MB, cationic dye) and congo red (CR, anionic dye), respectively, demonstrating a promising potential in environmental remediation. The maximum capacities of the monodispersed HAM@γ-AlOOH and HAM@γ-AlOOH/$Fe(OH)_3$ with hierarchical structures for MB and CR are determined at 87.80 mg g^{-1} and 252.53 mg g^{-1}. The adsorption capacities of the monodispersed HAM@γ-AlOOH and HAM@γ-AlOOH/$Fe(OH)_3$ with hierarchical structures for MB and CR in this study are higher than those of the other metal oxide nanostructures. The adsorption mechanism of the organic ions from solution is electrostatic attraction. In addition, the adsorption rates of MB and CR onto the monodispersed HAM@γ-AlOOH and HAM@γ-AlOOH/$Fe(OH)_3$ with hierarchical structures are rather fast. The underlying adsorption kinetics follow the pseudo-second-order model. Owing to their novel structures, special surface properties and high surface areas, both the two samples are

potentially applicable in water purification. This study also shows that the efficient adsorbents for organic pollution removal can be designed by depositing nanoparticles with high adsorption capacity on mesoporous supports with abundance of surface hydroxyls and large surface area.

Acknowledgements

This research was supported by the National Natural Science Foundation of China (51302102 51402120, 11504120, 51571166 and 61505167), the Natural Science Foundation of Anhui Province (1408085QA19), the Natural Science Research Project for Colleges and Universities of Anhui Province (KJ2014A222 and KJ2014B02), the Huaibei Scientific Talent Development Scheme (20140305), the Huaibei Normal University youth research project (2014xq001), the Doctor Foundation of Henan Institute of Engineering (D2014016) and the Key Scientific and Technological Team from innovation Shaanxi Province (No.2015KCT-12).

References

1. Y. Yin, R. M. Rioux, C. K. Erdonmez, S. Hughes, G. A. Somorjai and A. P. Alivisatos, *Science*, 2004, **304**, 711-714.
2. J. Hu, M. Chen, X. Fang and L. Wu, *Chem. Soc. Rev.*, 2011, **40**, 5472-5491.
3. X. W. Lou, L. A. Archer and Z. Yang, *Adv. Mater.*, 2008, **20**, 3987-4019.
4. Z. Wang, L. Zhou and X. W. Lou, *Adv. Mater.*, 2012, **24**, 1903–1911.
5. Z. Yin, Z. Wang, Y. Du, X. Qi, Y. Huang, C. Xue and H. Zhang, *Adv. Mater.*, 2012, **24**, 5374-5378.
6. Y. Liu, L. Yu, Y. Hu, C. Guo, F. Zhang and X. W. Lou, *Nanoscale*, 2011, **4**, 183-187.

7. D. Shujiang, C. Jun Song, Q. Genggeng, D. Xiaonan, W. Zhiyu, E. P. Giannelis, L. A. Archer and L. Xiong Wen, *J. Am. Chem. Soc.*, 2011, **133**, 21-23.

8. Y. Zhu, T. Ikoma, N. Hanagata and S. Kaskel, *Small*, 2010, **6**, 471-478.

9. J. G. Kim, S. M. Kim and I. S. Lee, *Small*, 2015, **11**, 1930-1938.

10. X. Zhang, J. Liu, S. Kelly, X. Huang and J. Liu, *J. Mater. Chem. A*, 2014, **2**, 11759-11767.

11. H. Chen, X. Wang, J. Li and X. Wang, *J. Mater. Chem. A*, 2015, **3**, 6073-6081.

12. E. M. Dias and C. Petit, *J. Mater. Chem. A*, 2015, DOI: 10.1039/C5TA05440K.

13. H. Jing, T. Wen, C. Fan, G. Gao, S. Zhong and A. W. Xu, *J. Mater. Chem. A*, 2014, **2**, 14563-14570.

14. K. T. Lee and S. Y. Lu, *J. Mater. Chem. A*, 2015, **3**, 12259-12267.

15. L. Wang, C. Cheng, S. Tapas, J. Lei, M. Matsuoka, J. Zhang and F. Zhang, *J. Mater. Chem. A*, 2015, **3**, 13357-13364.

16. S. Xing, D. Zhao, W. Yang, Z. Ma, Y. Wu, Y. Gao, W. Chen and J. Han, *J. Mater. Chem. A*, 2013, **1**, 1694-1700.

17. W. S. Wang, L. Zhen, C. Y. Xu, W. Z. Shao and Z. L. Chen, *Crystengcomm*, 2013, **15**, 8014-8021.

18. Y. Sun, B. Mayers and Y. Xia, *Adv. Mater.*, 2003, **15**, 641-646.

19. P. Jungwon, Z. Haimei, J. Young-wook and A. A Paul, *J. Am. Chem. Soc.*, 2009, **131**, 13943-13945.

20. M. Mo, J. C. Yu, L. Zhang and S. K. A. Li, *Adv. Mater.*, 2005, **17**, 756-760.

21. X. W. Lou and L. A. Archer, *Adv. Mater.*, 2008, **20**, 1853–1858.

22. M. Agrawal, S. Gupta, A. Pich, N. E. Zafeiropoulos and M. Stamm, *Chem. Mater.*, 2009, **21**,

5343-5348.

23. Q. Zhang, W. Wang, J. Goebl and Y. Yin, *Nano Today*, 2009, **4**, 494–507.

24. X. Y. Yu, L. Yu, L. Shen, X. Song, H. Chen and X. W. Lou, *Adv. Funct. Mater.*, 2014, **24**, 7440-7446.

25. X. Hong, C. Tan, J. Chen, Z. Xu and H. Zhang, *Nano Res.*, 2014, **8**, 40-55.

26. Z. Tierui, G. Jianping, H. Yongxing, Z. Qiao, A. Shaul and Y. Yadong, *Angew. Chem. Inter. Ed.*, 2008, **47**, 5806–5811.

27. X. Fang, Z. Liu, M. F. Hsieh, C. Mei, P. Liu, C. Cheng and N. Zheng, *Acs Nano*, 2012, **6**, 4434-4444.

28. Y. Wang, G. Wang, H. Wang, C. Liang, W. Cai and L. Zhang, *Chem Eur J.*, 2010, **16**, 3497–3503.

29. K. An and T. Hyeon, *Nano Today*, 2009, **4**, 359–373.

30. Y. Chen, H. Chen, L. Guo, Q. He, F. Chen, J. Zhou, J. Feng and J. Shi, *Acs Nano*, 2010, **4**, 529-539.

31. L. Tan, D. Chen, H. Liu and F. Tang, *Adv. Mater.*, 2010, **22**, 4885-4889.

32. T. Zhang, Q. Zhang, J. Ge, J. Goebl, M. Sun, Y. Yan, Y. S. Liu, C. Chang, J. Guo and Y. Yin, *J. Phys. Chem. C*, 2009, **113**, 3168-3175.

33. S. Liu, C. Chen, Q. Liu, Y. Zhuo, D. Yuan, Z. Dai and J. Bao, *RSC Advances*, 2015, **5**, 71728-71734.

34. Y. Xia, X. Jiao, Y. Liu, D. Chen, L. Zhang and Z. Qin, *J. Phys. Chem. C*, 2013, **117**, 15279-15286.

35. W. Cai, J. Yu, B. Cheng, B. L. Su and M. Jaroniec, *J. Phys. Chem. C*,2009, **113**,

14739-14746.

36. E. Kumar, A. Bhatnagar, W. Hogland, M. Marques and M. Sillanpää, *Chem. Eng. J.*, 2014, **241**, 443-456.

37. A. J. McCue, A. M. Shepherd and J. A. Anderson, *Catalysis Sci. Tech.*, 2015, **5**, 2880-2890.

38. W. Cai, J. Yu and M. Jaroniec, *J. Mater. Chem.*, 2010, **20**, 4587-4594.

39. T. Kim, J. Lian, J. Ma, X. Duan and W. Zheng, *Cryst.Growth Des.*, 2010, **10**, 2928-2933.

40. Y. Zhu, H. Hou, G. Tang and Q. Hu, *Eur. J. Inorg. Chem.*, 2010, **6**, 872–878.

41. J. Zhang, S. Wei, L. Jing, J. Luo, S. Liu, H. Song, E. Elawad, X. Ding, J. Gao and S. Qi, *J. Phys. Chem. B*, 2006, **110**, 21680-21683.

42. Y. X. Zhang, Y. Jia, Z. Jin, X. Y. Yu, W. H. Xu, T. Luo, B. J. Zhu, J. H. Liu and X. J. Huang, *Crystengcomm*, 2012, **14**, 3005-3007.

43. H. Liang, L. Liu, H. Yang, J. Wei, Z. Yang and Y. Yang, *Crystengcomm*, 2011, **13**, 2445-2450.

44. H. Huang, L. Wang, Y. Cai, C. Zhou, Y. Yuan, X. Zhang, H. Wan and G. Guan, *Crystengcomm*, 2015, **17**, 1318-1325.

45. W. Cai, J. Yu and S. Mann, *Microporous Mesoporous Mater.* 2009, **122**, 42–47.

46. D. H. Buchold and C. Feldmann, *Nano Lett.*, 2007, **7**, 3489-3492.

47. Q. Feng, Z. Zhang, Y. Ma, X. He, Y. Zhao and Z. Chai, *Nanoscale Res. Lett.*, 2012, **7**, : 84.

48. C. Lin, Y. Li, M. Yu, P. Yang and J. Lin, *Adv. Funct. Mater.* 2007, **17**, 1459–1465.

49. X. H. Li, Y. X. Zhang, Z. L. Liu, Q. Z. Liu, B. Li, G. P. Zhu and K. Dai, *Rsc Adv.*, 2014, **4**, 62209-62214.

50. Y. X. Zhang, X. Y. Yu, Z. Jin, Y. Jia, W. H. Xu, T. Luo, B. J. Zhu, J. H. Liu and X. J. Huang, *J. Mater. Chem*, 2011, **21**, 16550-16557.

51. W. Zhu, L. Zhang, G. L. Tian, R. Wang, H. Zhang, X. Piao and Q. Zhang, *Crystengcomm*, 2013, **16**, 308-318.

52. Z. Jian, W. Songling, X. Songhai and L. Hexing, *Chem. Commun.*, 2011, **47**, 4403-4405.

53. T. S. Natarajan, H. C. Bajaj and R. J. Tayade, *J. Colloid Interface Sci.,* 2014, **433**, 104–114.

54. H. Chen and J. He, *J. Phys. Chem. C*, 2008, **112**, 17540-17545.

55. F. Jing, Y. Wang, L. Zou, B. Li, X. He, Y. Ren, Y. Lv and Z. Fan, *J. Colloid Interface Sci.,* 2015, **438**, 318–322.

56. W. Cai, Y. Hu, J. Chen, G. Zhang and T. Xia, *Crystengcomm*, 2012, **14**, 972-977.

57. C. Wang, Y. Le and B. Cheng, *Ceram. Int.,* 2014, **40**, 10847–10856.

58. J. B. Fei, Y. Cui, X. H. Yan, W. Qi, Y. Yang, K. W. Wang, Q. He and J. B. Li, *Adv. Mater.*, 2008, **20**, 452-456.

59. C. Yu, X. Dong, L. Guo, J. Li, F. Qin, L. Zhang, J. Shi and D. Yan, *J. Phys. Chem. C*, 2008, **112**, 13378-13382.

60. Y. X. Zhang and Y. Jia, *Appl. Surface Sci.*, 2014, **290**, 102-106.

61. C. Y. Kuo and H. Y. Lin, *Desalination*, 2009, **249**, 792–796.